Nanopore tweezers: Voltage-controlled trapping and releasing of analytes

Mauro Chinappi*
Center for Life Nano Science@Sapienza, Istituto Italiano di Tecnologia, Via Regina Elena 291, 00161 Roma, Italia

Tudor Luchian
Department of Physics, Laboratory of Molecular Biophysics and Medical Physics, Alexandru I. Cuza University, Iasi 700506, Romania

Fabio Cecconi
CNR-Istituto dei Sistemi Complessi UoS "Sapienza," Via dei Taurini 19, 00185 Roma (Italy)
(Received 13 May 2015; revised manuscript received 3 June 2015; published 15 September 2015)

Several devices for single-molecule detection and analysis employ biological and artificial nanopores as core elements. The performance of such devises strongly depends on the amount of time the analytes spend into the pore. This residence time needs to be long enough to allow the recording of a high signal-to-noise ratio analyte-induced blockade. We propose a simple approach, dubbed nanopore tweezing, for enhancing the trapping time of molecules inside the pore via a proper tuning of the applied voltage. This method requires the creation of a strong dipole that can be generated by adding a positive and a negative tail at the two ends of the molecules to be analyzed. Capture rate is shown to increase with the applied voltage while escape rate decreases. In this paper we rationalize the essential ingredients needed to control the residence time and provide a proof of principle based on atomistic simulations.

DOI: 10.1103/PhysRevE.92.032714 PACS number(s): 87.80.Nj, 37.10.Pq, 87.85.Qr

I. INTRODUCTION

In recent years, a wide number of nanopore-based devices for the analysis of macromolecules have been proposed in literature [1–10]. Their working principle is definitely simple: The single macromolecule capture and subsequent translocation through the nanopore, induced by an applied membrane potential, depend upon the physicochemical and topological features of the analyte, so, in principle, the identity, the concentration, and other microscopic properties of the analyte (e.g., diffusion coefficient, volume, and charge) can be inferred from the analysis of the stochastic current blockades determined by the analyte-nanopore interaction [1,2,11]. Nanopore-based sensing protocols have found a large number of applications such as nucleic acid sequencing [12,13] and peptide folding analysis [8,14,15]. This experimental activity stimulated several theoretical and computational approaches to describe capture and transport mechanisms [16–20] and to establish a correlation between current values and macromolecule conformations in the pore [5,21–23].

In general, a nanopore sensor has to fulfill two technical requirements: a high signal-to-noise ratio, in order to discriminate the pulses of electric current from the background noise, and a sensitivity able to resolve different elements that transit at a given time along the pore. A major limitation which is common to both biological and solid-state nanopore sensors consists in the short time an analyte spends inside them. Several different methods have been recently proposed to control the translocation and to increase the residence time of analytes. Those methods are based on modifications of the pore [24–26], of the flow [27,28], of the electrolyte [29], or of the translocating molecule [3,6,30].

In this paper we rationalize and extend an approach [31], dubbed *nanopore tweezer*, to control the residence time of a molecule inside a nanopore. The method can be applied to both biomolecules and nanoparticles. The only requirement is the strong polarity of particles (or molecules) to be analyzed, a condition that can be artificially obtained, for instance, by adding a positive and a negative tail to the opposite ends of it. In Sec. II the generic principle of the nanopore tweezer is discussed. Explicit calculation for a toy-model (a rigid rod engaging a cylindrical nanopore) is presented in Sec. III for a symmetric and an asymmetric case. Finally, a proof of principle based on all-atom molecular dynamics simulations is shown in Sec. IV.

II. NANOPORE TWEEZER PRINCIPLE

Let us consider a nanopore separating an electrolytic cell in two chambers, cis and trans, respectively, and let $\Delta V = V_{\rm cis} - V_{\rm trans}$ be the applied voltage across the cell. The presence of the nanopore results in an inhomogeneous electrical field $\mathbf{E}(\mathbf{x}) = -\nabla V$, see Fig. 1(a). Although the shape of $\mathbf{E}(\mathbf{x})$ depends on the specific system features, such as the pore geometry and the surface charge, in general, $\mathbf{E}(\mathbf{x})$ is much more intense inside the pore and it rapidly decreases outside (see, e.g., Refs. [32,33] and Appendix A).

A neutral, but strongly polar, molecule on the cis side tends to align to $\mathbf{E}$ and, due to the field variation, experiences a small but non-negligible force that drives it towards the pore entrance. Assuming, without loss of generality, a positive ΔV, as soon as the molecule enters the pore, its positively charged tail undergoes a gradually increasing importing force. However, as the translocation proceeds, its negative charged tail starts feeling a force directed towards the cis side. As a result, the total force on the molecule decreases until it establishes an equilibrium where positive and negative actions balance and the molecule remains trapped in the middle of

*mauro.chinappi@iit.it

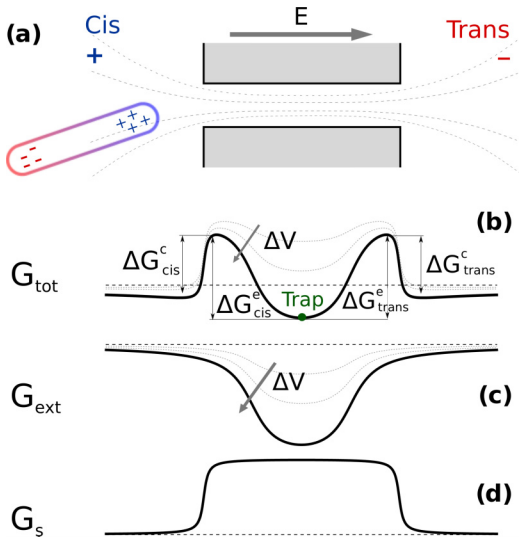

FIG. 1. (Color online) General scheme of the nanopore tweezer. A voltage ΔV is applied between cis and trans compartments. An inhomogeneous electric field $\mathbf{E}$ sets in [dashed lines in (a)]. $|\mathbf{E}|$ is larger inside the pore and goes to zero far from the pore. A polar particle in the cis compartment is attracted towards the pore entrance. The electric contribution to the free energy due to ΔV and the entropic one are qualitatively sketched in panels (c) and (d). The combination of the twos results in $G_{\rm tot}$, see panel (b). The capture $(\Delta G^c_{\rm cis}, \Delta G^c_{\rm trans})$ and escape $(\Delta G^e_{\rm cis}, \Delta G^e_{\rm trans})$ barriers are functions of ΔV. The profiles refer to a symmetric case where barriers at cis and trans sides are identical; however, asymmetries in the system result in unbalance between cis and trans behaviors.

the pore. Any displacement toward either the cis side or the trans side results in a net restoring force bringing it back to the equilibrium (zero force) state.

Besides the action of the applied voltage ΔV, other factors affect the molecule dynamics. To enter the pore, the molecule has to overcome a free-energy barrier associated with the entropy cost of the confinement. Hence, the capture and the trapping are the result of a subtle competition between entropy and electrostatic energy as shown in the cartoon representation of Fig. 1. As we will focus on the general mechanism, we shall neglect all those effects that could be problem specific, such as the interaction between the particle and the pore or between the particle and the fluid (electro-osmosis, see, e.g., Refs. [6,34–37]).

In a first approximation, we can express $G_{\rm tot}$ as the sum of two independent terms, $G_{\rm ext}$ due to the applied voltage and the contribution G_s associated with entropic penalty of the confinement into the pore. Generally, G_s is negligible outside the pore and increases with the molecule approaching it, see Fig. 1(d), while $G_{\rm ext}$ has a minimum inside the pore, see Fig. 1(c). Their combination, $G_{\rm tot} = G_s + G_{\rm ext}$, results in a profile like that sketched in Fig. 1(b). In practice, the molecule is expected to overcome a capture barrier to enter the pore, soon after it gets trapped in the minimum of $G_{\rm tot}$ and has to pay a further free-energy cost to escape. This simple mechanism realizes the tweezing principle.

Summarizing, the general ingredients of the nanopore tweezers are (i) nonhomogeneous electrical field $\mathbf{E}(\mathbf{x})$ induced by the nanopore in presence of an applied voltage ΔV and (ii) a translocating particle with a strong dipole moment. In the following section these intuitive considerations will be made more quantitative with the introduction of a simple model through which we study the interplay between the basic ingredients of the nanopore tweezers and the stability against thermal fluctuations.

III. MODEL OF NANOPORE TWEEZERS

In the following, to describe the main scenarios that can occur in a nanopore tweezer, we present theoretical results from a model system where the translocating particle is portrayed as a cylindrical rod of length L_r and diameter d_r with a charge distribution $\rho(\xi)$, where $\xi \in (-L_r/2, L_r/2)$ is a coordinate on the rod, Fig. 2(a). The rod center of mass, indicated as x_g, is chosen as a collective variable, hence the final purpose of our analysis is to derive the free-energy profile $G_{\rm tot}(x_g)$. The pore is a cylinder of diameter d that spans the region $x \in (-L/2, L/2)$. We work under the following assumptions: (i) the electrical potential $V(x)$ generated by the applied external voltage ΔV is not affected by the presence of the rod; (ii) the charge distribution on the rod, $\rho(\xi)$, is not affected by the electrical field $\mathbf{E}(\mathbf{x})$; and (iii) $V(x)$ is proportional to ΔV. Without loss of generality, the cis side is toward $x < 0$ while the trans side is for $x > 0$ and ξ is oriented in the same direction of the x axis, i.e., from cis to trans.

Hereafter, we work in dimensionless units such that $k_B T = 1$, the pore length is $L = 1$, and the electron charge is $e = 1$. As a consequence, the free-energy barriers ΔG are measured in $k_B T$ units.

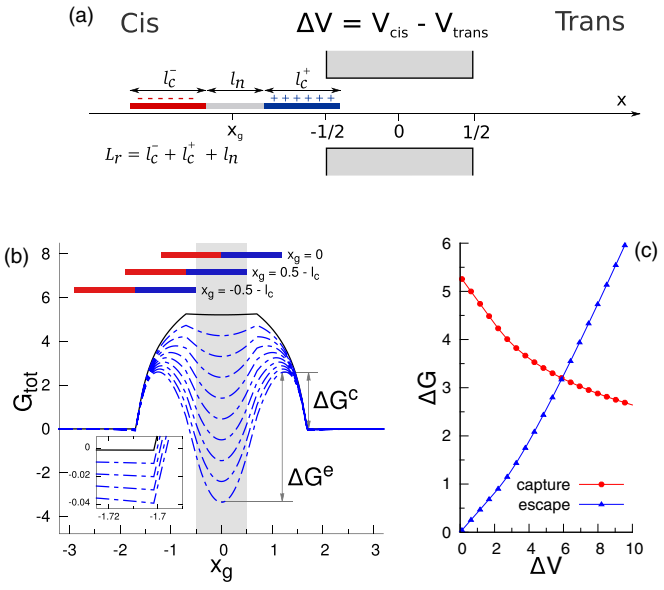

FIG. 2. (Color online) Model system for nanopore tweezer. (a) A rod with the two ends oppositely charged moves along the x axis. (b) Free-energy profile $G_{\rm tot}(x_g)$ as a function of the rod center x_g ($l_c^+ = l_c^- = L_r/2 = 1.2$, $d = 0.2$, $d_r = 0.1$). ΔV increases from black (solid) to blue (dashed) curves. The gray shaded area corresponds to the pore region. (c) Capture and escape barriers as functions of ΔV.

The rod is positively charged [$\rho(\xi) = 1$] for $\xi > 0$ and negatively charged [$\rho(\xi) = -1$] for $\xi < 0$, with l_c^+,l_c^- being the length of the positive and negative tails while the length of the central neutral region is indicated by l_n, see Fig. 2(a). The electrical contribution to the total free energy $G_{\rm tot}(x_g)$ amounts to

$$G_{\rm ext}(x_g) = \int_{-\infty}^{+\infty} dx\ V(x)\rho(x - x_g). \tag{1}$$

The detailed shape of $V(x)$ is discussed in Appendix A; in a nutshell, we treat the pore and the solution inside as a cylindrical conductor, while the two pore entrances are modelled as hemispherical electrodes of diameter d, as in Ref. [32].

In addition, we assume that entropic contribution is mainly orientational. Indeed, when the rod has an end placed at the pore entrance, its opposite end can freely span a half sphere, whereas if the rod is either partially or completely inserted into the pore, its allowed orientations are drastically reduced, yielding a free-energy term,

$$G_s(x_g) = -k_B T \log \frac{\Omega(x_g)}{2\pi}, \tag{2}$$

where $\Omega(x_g)$ is the solid angle which the rod can access to when it partially occupies the pore, whereas 2π is the solid angle that the rod can span when its terminal lies at the pore entrance. The quantity $\Omega(x_g)$ of course depends on geometrical properties of the pore and the rod as well. The case of a cylindrical rod of diameter d_r and length L_r, and a cylindrical pore of diameter d and length L, corresponds to

$$\Omega(x_g) \simeq 2\pi \left(1 - \frac{L_e}{\sqrt{L_e^2 + d_e^2}}\right),$$

where $d_e = d - d_r$, is the effective pore diameter and L_e is the portion of the rod inside the pore, see Appendix B.

This simplified model, which specifically refers to rod-like molecules, with large persistence length, may be even extended, upon the necessary corrections, to flexible and not-too-long chains. Indeed, the artificial dipole imposed to the molecules confers a certain degree of stiffness to them, as they will tend to straighten under the effect of the local electric field. In such conditions, the highest entropy of more flexible chains can be balanced by a proper increase of ΔV to maintain the deepness of the central minimum in the free-energy profile. Obviously for large biomolecules the theory needs a refinement to account for more accurate expressions of the confinement entropy loss [38–40], even if we expect the general mechanism still to hold. In the most complex and general cases where no expressions for the conformational entropy are available, one can certainly resort to standard Monte Carlo or Molecular Dynamics techniques which allow the free-energy profiles to be reconstructed in the proper collective variable [41–44] and verify whether the tweezing effect is still applicable.

A. Charged symmetric rod

We start our analysis by considering a symmetric system consisting of a cylindrical pore of diameter $d = 0.2$ and a globally neutral symmetric rod without the uncharged region in the middle: $l_n = 0$ and $l_c^+ = l_c^- = L_r/2 \equiv l_c$. The tweezing mechanism is well illustrated by both the shape and the changes of free-energy profiles $G_{\rm tot}$ upon varying ΔV, reported in Fig. 2(b) with evident similarity to the qualitative scenario of the competition between electrostatic energy and entropy discussed in Fig. 1(b).

At zero voltage [black solid line in Fig. 2(b)] the free energy is a pure entropic barrier with a plateau in the middle. The modulation the profiles undergo when the voltage is switched on can be explained by considering the positions assumed by the rod with respect to the pore center in the tweezing process. When the rod is on the cis side, it is constantly attracted towards the pore entrance, thus $G_{\rm tot}$ decreases, reaching a local minimum at $x_g = -0.5 - l_c$, i.e., when the rod trans end is located at the cis pore mouth, see Fig. 2(b). From that position, any displacements towards the trans side increases $G_{\rm tot}$; indeed, the entropic gain exceeds the $G_{\rm ext}$ loss and a maximum is attained when the pore is fully occupied by the rod, $x_g = 0.5 - l_c$. Further motion of the rod towards the trans side involves only energy contributions as the entropy variation is zero, and, as a consequence, the free energy decreases, reaching a minimum when the rod occupies the center of the channel $x_g = 0$. The symmetry of the problem implies equivalent maximum and minimum also at the trans side. The system, hence, shows three minima, two at the pore ends and one corresponding to the molecule trapped in the middle of the pore. As ΔV increases all the three minima become deeper and deeper, although the variation are much more marked for the central minimum, the only one that matters to the tweezing effect. The tweezing is actually fully achieved at those ΔV values that determine a stability of the central well beyond the thermal fluctuations.

Figure 2(c) reports the capture ΔG^c and the escape ΔG^e barriers as functions of ΔV, showing that the capture mechanism is enhanced while the escape process is depressed when ΔV increases, so the tweezer is stable. This behavior of the free-energy barriers is in qualitative agreement with the results of Asandei *et al.* [31] for a peptide chain, suggesting that the tweezer effect may occur independently on the details of the entropic and electrical contributions to $G_{\rm tot}$.

Changing the rod length L_r, other regimes occur. They are characterized by a qualitatively different shape of the $G_{\rm tot}$ where additional minima and maxima appear for specific ranges of ΔV. The data are reported in the Supplemental Material, Fig. S1 [45]. Although those additional minima and maxima modify the shape of the profile, they are associated to barriers much smaller than $k_B T$, and, consequently, they are not expected to play a role in the molecule trapping.

B. Charged asymmetric rod

The symmetry between the cis and trans escape barriers can be broken by introducing an unbalance in the charge distribution of the rod. More specifically, with respect to a reference symmetric case $l_{c,0}^+ = l_{c,0}^- = l_n = L_r/3 = 0.8$, we altered the tail lengths, $l_c^+ > l_c^-$, while keeping the length of the neutral region constant and the other parameters unchanged.

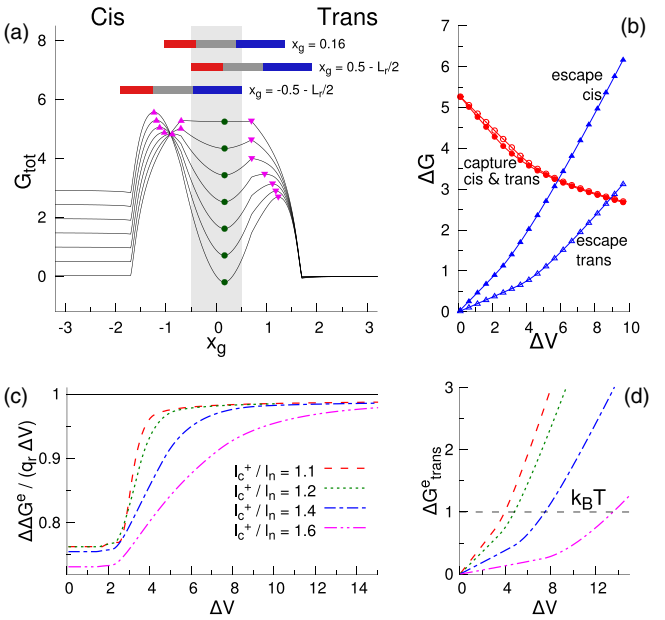

FIG. 3. (Color online) Asymmetric case. (a) Free energy $G_{\rm tot}(x_g)$ for $L_r = 2.4$, $l_c^+ = 0.96$, $l_c^- = 0.64$. Each curve corresponds to a different ΔV, magenta triangles indicate the cis and trans maxima while the green circles indicate the minimum at $x_g \simeq (l_c^+ - l_c^-)/2 = 0.16$. (b) Escape (blue triangles) and capture (red circles) barriers as functions of ΔV for the cis and trans sides. (c) Difference in cis and trans escape barriers, $\Delta\Delta G^e$, for different charge unbalances. (d) Trans escape barrier, the color code is the same as in panel (c).

This implies that now the rod has a net positive charge $q_r = l_c^+ - l_c^-$ [1].

Figure 3(a) shows the $G_{\rm tot}(x_g)$ profile for $l_c^+/l_n = 1.2$ where one can appreciate the difference behavior of the values at the cis and trans sides. This asymmetry results in a net attraction exerted on the positively charged rod ($q_r > 0$) by the negative electrode. As a consequence, the minimum in $G_{\rm tot}$ is no longer located at $x_g = 0$ but is shifted toward the trans side. Indeed, in a first approximation, equilibrium requires that the portion of the rod inside the pore has zero charge, a condition that, in our case, is attained when the center of the neutral region is aligned with the pore center. Thus, geometric considerations lead to the value $x_{g,\rm min} \simeq 1/2(l_c^+ - l_c^-)$ for the minimum of the free energy. More importantly, the cis escape barrier is greater than the trans one, implying that, once captured, the rod will preferentially escape towards the trans side.

Figure 3(c) reports the difference between cis and trans escape barriers, $\Delta\Delta G^e = \Delta G^e_{\rm cis} - \Delta G^e_{\rm trans}$, normalized to the energy $q_r\Delta V$, which represents the difference between the free-energy bulk values, $G_{\rm tot}(-\infty) - G_{\rm tot}(\infty)$. For high ΔV, the predominance of the electric over the entropic contribution makes all the curves tend to a plateau value $q_r\Delta V$, i.e., to the difference between the bulk values of the free energy. At low voltages another plateau occurs, whose value can be estimated by assuming that in the subtraction, $\Delta G^e_{\rm cis} - \Delta G^e_{\rm trans}$, the entropy terms cancel out with a good accuracy due to the symmetry of the entropy profile. Concerning the cis side, the escape barrier can be estimated as

$$\Delta G^e_{\rm cis} = G_{\rm ext}\left(x^{\rm cis}_{g,\rm max}\right) - G_{\rm ext}(x_{g,\rm min}),$$

where $x^{\rm cis}_{g,\rm max} \simeq -0.5 - L_r/2$ indicates the maximum on the cis side. Assuming that the voltage drop occurs mainly inside the pore, simple but tedious integration of Eq. (1) provides the result $\Delta G^e_{\rm cis} \simeq \Delta V (l_c^+)^2/2$. Applying the same argument to the trans side, we find $\Delta G^e_{\rm trans} \simeq \Delta V (l_c^-)^2/2$ and, consequently,

$$\Delta\Delta G^e \simeq \frac{(l_c^+ + l_c^-)}{2}(l_c^+ - l_c^-)\Delta V \simeq 0.8 q_r \Delta V, \qquad (3)$$

in fair agreement with numerical data.

As a final comment, we observe that the escape barrier decreases as the asymmetry increases, see Fig. 3(d). This means that the charge unbalance reduces the tweezer effect, a result recently observed in experiments on peptide translocation through a biological nanopore [46].

IV. MOLECULAR DYNAMICS SIMULATIONS

Finally, as a proof of principle, we performed all-atoms molecular dynamics (MD) simulations of a rod of length $L_r \simeq 78$ Å with $l_c^- = l_c^+ = L_r/3$ in a pore of length $L \simeq 68$ Å and diameter $d \simeq 7$ Å. The runs were performed using the NAMD package [47] while VMD [48] was employed for system preparation, data analysis, and image rendering. The rod is modelled as Lennard-Jones atoms arranged on a series of tetrahedra with side $a = 2$ Å, see Fig 4(a). Topotools[2] was employed to generate the structure file for the rod where only the bonds corresponding to the tetrahedra sides were included [red bond in Fig. 4(a)]. To guarantee the proper rigidity to the rod, we added extra bonds between the bases of consecutive tetrahedra, such as B13–B23 and B13–B21, and between atoms on the rod axis as well, such as C1–C2. Moreover, a dihedral potential enforces the angle between corresponding faces of specular tetrahedra, e.g., C2-B23-B12-C3, yellow triangle in Fig. 4(a). The rod is constituted by 97 atoms corresponding to 24 consecutive tetrahedra plus a final tip atom for a total length of 78.4 Å. The atoms at the ends of the rod carry charges with opposite sign. The pore is generated following the approach proposed in Refs. [21,49,50] and reported in the bionanotechnology-tutorial by Aksimentiev and Comer[3] for the SiN pore. However, in order to keep out surface charge effects, we set the atomic charges of the pore atoms to zero. The reference system is placed on the pore center with the z axis aligned to the pore axis. The pore length is ≃68 Å, i.e., the pore goes from $z \simeq -34$ Å to $z \simeq 34$ Å, while its diameter is ≃7 Å. Water and ions are added using VMD, resulting in a complete system of 196 421 atoms. Periodic boundary conditions were applied in all the directions; in particular, on the Oxy plane hexagonal periodicity is employed. Water and KCl ions (0.2 M) are modelled following

[1] We note that we are working in dimensionless units.

[2] https://sites.google.com/site/akohlmey/software/topotools

[3] http://bionano.physics.illinois.edu/tutorials/bionanotechnology-tutorial

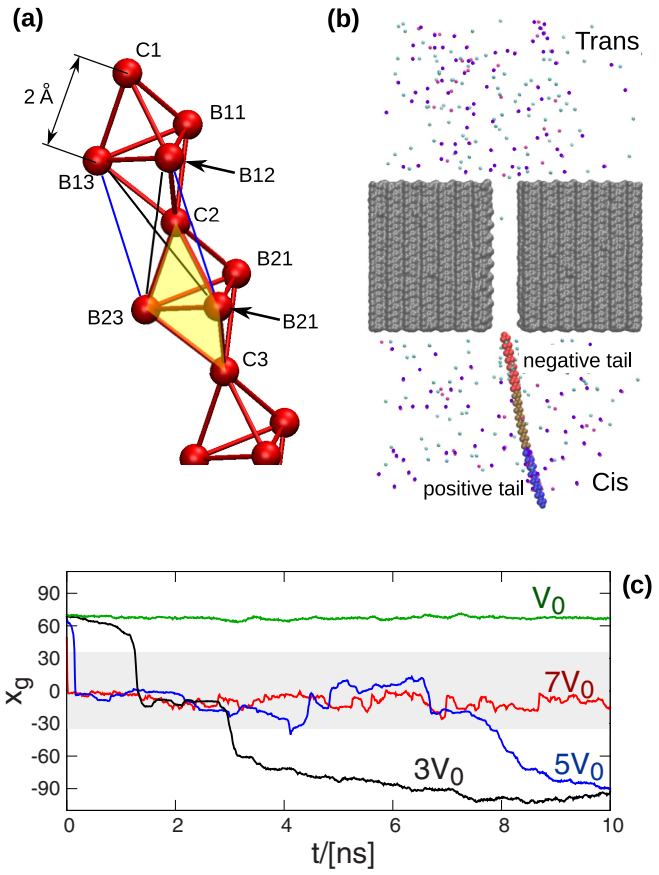

FIG. 4. (Color online) Molecular dynamics simulation setup and results. The rod structure is shown in panel (a), while panel (b) reports the simulation setup. The snapshot is taken after the equilibration. The pore is reported in gray (only a section around Ozx plane was drawn), while the positive and the negative tails of the rod are reported in red and blue, respectively. Water molecules are not shown while Cl^- and K^+ ions are in cyan (light gray) and violet (dark gray). (c) Time evolution of the rod center of mass x_g for four different voltages (V_0, $3V_0$, $5V_0$, $7V_0$, see labels on the curves, with $V_0 = 9.03V$). The gray shaded area corresponds to the pore region.

the standard CHARMM36 strategy including the NBFIX modification for ions [51].

A first isothermal-isobaric (NPT) run is performed to equilibrate the system. During this stage only L_z is allowed to vary, reaching a final value of 207.2 Å. The rod tip is constrained at the pore entrance by means of a harmonic spring centered in (0,0,35) Å and also the membrane atoms are constrained to their initial positions. After equilibration, the constraint on the rod is removed and a homogeneous electric field $\mathbf{E} = (0,0,E_z)$ is applied to the system. As shown in Ref. [52], this is equivalent to the application of a constant voltage $\Delta V = E_z L_z$.

Figure 4 reports the time course of the rod center of mass x_g for four different applied voltages. At the lowest ΔV (green curve), the rod is not captured by the pore in the allotted time window of 10 ns. In contrast, for high voltages (red curve), the rod is suddenly captured and it is not able to escape. Mixed scenarios are possible at intermediate voltages, where the rod is first captured and then released (blue and black curves). It is apparent that the residence time increases with voltage, in agreement with the prediction of the toy model discussed in previous sections.

V. CONCLUSIONS

In this paper we described an approach, dubbed *nanopore tweezer*, for trapping an analyte inside the pore and controlling its residence time via a proper tuning of the applied voltage. The approach requires a certain polarity of the molecule, a condition that can be realized, for instance, by adding positive and negative tails to the two ends of the molecule of interest, as shown in Ref. [31] for peptides. The applied potential ΔV induces a nonhomogeneous electrical field that is more intense inside the pore. The artificial polarity of the molecules favors their capture as their dipole tends to align along the field lines that converge into the pore. Specifically, as soon as the molecule enters the pore, it experiences a gradually increasing importing force due to the larger electrical field. When also the other charged tail engages the pore, an opposite couple of forces generates a sort of "tug-of-war" for which the analyte becomes stably trapped in the middle of the pore. Since the intensity of the electrical field can be controlled by changing ΔV, both capture and escape rates can be easily and properly tuned. In particular, the capture rate increases with voltage while the escape rate decreases.

This feature can be exploited for a novel nanopore sensing approach where the residence time can be controlled "on demand" as shown in Fig. 5. For low voltages, $t < t_1$, the current is low and no capture takes place: Low voltage implies a high capture barrier. An increase of the voltage, while enhancing the ionic current, decreases the capture barrier, making the import process of the analyte into the pore highly

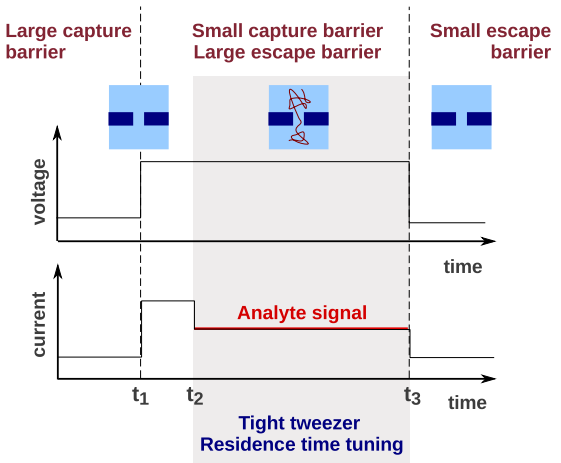

FIG. 5. (Color online) Sketch of a possible application of the nanopore tweezer for on-demand selection of the analyte residence time. The applied voltage is increased at time t_1. This results in a large ionic current, $t \in (t_1,t_2)$. However, high voltage results also in a reduction of the capture barrier, hence the analyte, after some delay, is captured by the pore at $t = t_2$ and the ionic current alteration induced by the analyte is observed, $t \in (t_2,t_3)$. Large escape barriers trap the analyte inside the pore sensing region. When a long-enough signal is recorded, the voltage is reduced and the analyte suddenly escapes ($t = t_3$).

probable, $t = t_2$. Once captured, the high escape barriers trap the molecule inside the nanopore. After the recording of a sufficiently long current signal, the applied voltage can be reduced and, consequently, the molecule is released, $t = t_3$. The probability to exit from the cis site or from the trans site can be controlled by introducing an asymmetry in the system. Biological pores usually present a natural asymmetry as they carry a not uniform charge that can be also influenced by the pH conditions. However, as we have shown, the asymmetry can be also induced by a proper unbalance between the positively and negatively charged tails of the translocating molecule.

In this work we rationalized the fundamental ingredients needed to setup a nanopore tweezer and discussed, via a simple one-dimensional (1D) model of a rigid rod translocating across a cylindrical pore, some of the different scenarios that take place by varying the polarity of the particle. We also explored the effect of the asymmetry in cis and trans escape barriers, showing that, in general, the asymmetry reduces the tweezer effectiveness but allows the preferred escape direction to be selected. This result agrees with recent findings where asymmetry was induced by salt gradients [31] or pH differences [46] and suggests that the reduction of the residence time in the pore with the asymmetry is a general property of the nanopore tweezer. We expect this simple and versatile technique to be useful for a wide class of nanopore-based analysis, ranging from biopolymers to nanoparticles, such as bipolar Janus particles [53] with different charges on the two halves or dielectric particles.

ACKNOWLEDGMENTS

This research used the computational resources of the PRACE Project No. 2014112673 (TGCC Curie, France) and ISCRA_C MUGRA (CINECA). T.L. acknowledges the financial support offered by Grants No. PN-II-ID-PCCE-2011-2-0027 and No. PN-II-PT-PCCA-2011-3.1-0595 and National Research Foundation of Korea (NRF), Global Research Laboratory (GRL) Grant No. NRF-2014K1A1A2064460.

APPENDIX A: MODEL FOR $V(x)$

To estimate the general potential $V(\mathbf{r})$ inside and outside the nanopore, we followed the approach proposed by Wanunu *et al.* [32] adapted to our system. As a first step, let us recall the derivation of the potential generated by a spherical electrode of diameter d placed at the origin of the reference frame and surrounded by a medium of conductivity σ. Let $\delta V = V_{\text{ele}} - V_{\infty}$ be the applied voltage assumed constant in time. The spherical symmetry of the problem allows the overall resistance to be written as

$$R = \int_{d/2}^{\infty} dr \, \frac{1}{4\sigma\pi r^2} = \frac{1}{2\sigma\pi d}, \tag{A1}$$

with $r = |\mathbf{r}|$ being the distance from the electrode center. If a current I is assumed to flow from the electrode to the infinity, from the Ohm's law, we obtain

$$\delta V = \frac{I}{2\sigma\pi d}. \tag{A2}$$

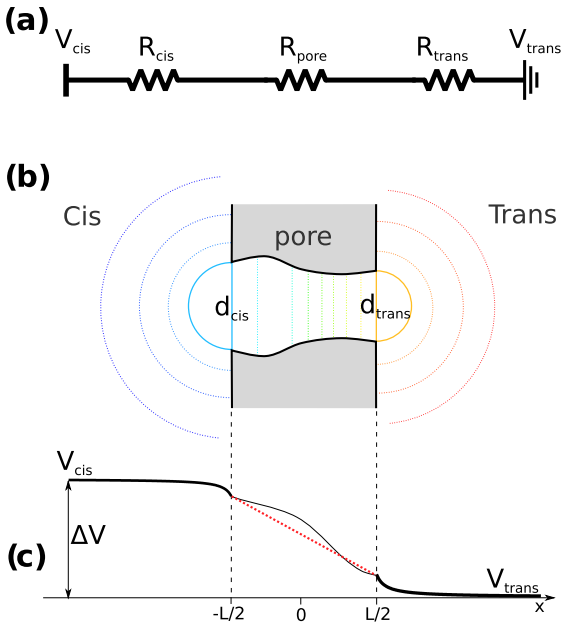

FIG. 6. (Color online) Potential inside and outside the pore. In the simplest approximation the system is described as a series of three resistances R_{cis}, R_{pore}, and R_{trans} panel (a). The electrical current I is hence, $I = \Delta V/(R_{\text{cis}} + R_{\text{pore}} + R_{\text{trans}})$, with $\Delta V = V_{\text{cis}} - V_{\text{trans}}$. The isolines of the potential $V(\mathbf{r})$ are qualitatively reported as dashed lines panel (b). The pore mouths are modelled as hemispherical electrodes, and $V(\mathbf{r})$ isolines are hemispherical with the electrical field $\mathbf{E} = -\nabla V$ radial respect to the center of the pore mouth. A 1D model is employed for the pore with $V(\mathbf{r})$ isolines normal to the pore axis, electrical field $\mathbf{E} = -\nabla V$ parallel to the pore axis and constant on the pore section is employed for the pore. Panel (c) reports the electrical potential field on the pore axes. The great part of the potential drop occurs in the pore. Note that if the pore is a cylinder, the potential between $-L/2$ and $L/2$ is linear (red dashed line). It is worth noting that in several experimental works the cis side is grounded and not the trans side. This different convention does not affect the tweezing mechanism discussed in the present paper.

Moreover, since the current I is constant, it is possible to resort to the differential form of Ohm's law, $dV = I\,dR$, written as

$$\frac{dV}{dr} = \frac{I}{4\sigma\pi r^2}, \tag{A3}$$

which, integrated from r to $r = \infty$, yields

$$V_{\infty} - V(r) = \int_{r}^{\infty} \frac{I}{4\sigma\pi r^2}\, dr = -\frac{I}{4\sigma\pi r}, \tag{A4}$$

i.e.,

$$V(r) = \frac{I}{4\sigma\pi r} - V_{\infty}. \tag{A5}$$

Our nanopore device can be described as a series of three blocks, the cis side, the channel, and the trans side. The cis and trans sides are modelled as half-spherical electrodes of diameter d_{cis} and d_{trans} [continuous bold lines in Fig. 6(b)]. This implies that their resistance amounts to

$$R_{\text{cis}} = \frac{1}{\pi\sigma_{\text{cis}} d_{\text{cis}}}, \qquad R_{\text{trans}} = \frac{1}{\pi\sigma_{\text{trans}} d_{\text{trans}}}. \tag{A6}$$

where $\sigma_{\rm cis}$ and $\sigma_{\rm trans}$ are the conductivities at the cis and trans sides.

The pore is assumed to be an ideal cylinder around the x axis filled with a medium of local conductance $\sigma(x)$, so, according to Ohm's second law, its overall resistance is given by the integral

$$R_{\rm pore} = \int_{-L/2}^{L/2} \frac{dx}{\sigma(x)S(x)}, \tag{A7}$$

with $S(x)$ indicating the pore section, and

$$\frac{dV}{dx} = \frac{I}{\sigma(x)S(x)}. \tag{A8}$$

Note that, in general, the conductivity of the electrolyte can change along the pore; typical examples are when the cis and trans salt concentrations differ or when the pore surface is strongly charged. The total resistance of the system is given by $R_{\rm tot} = R_{\rm cis} + R_{\rm trans} + R_{\rm pore}$, and hence the electric current is

$$I = \frac{\Delta V}{R_{\rm tot}}. \tag{A9}$$

In the simplest case of homogeneous conductivity $\sigma(x) = \sigma$ and cylindrical pore of diameter d the following simplifications hold:

$$R_{\rm cis} = R_{\rm trans} = \frac{1}{\pi\sigma d}, \qquad R_{\rm pore} = \frac{4L}{\pi\sigma d^2}, \tag{A10}$$

hence

$$I = \frac{\Delta V}{R_{\rm tot}} = \Delta V \frac{\pi\sigma d}{2}\left(\frac{d}{2L+d}\right). \tag{A11}$$

Given the constant value of I, a direct integration of (A8) and (A3) provides $V(\mathbf{r})$ in the cis, trans, and pore regions. The problem is determined once the boundary conditions at $\pm\infty$ are also taken into account; without loss of generality we consider: $V_{\rm cis} = \Delta V$ and $V_{\rm trans} = 0$. The only remaining issue concerns the matching of the solutions at the boundaries of the mentioned regions. Since there is a certain degree of arbitrariness, here we can assume that the potential for the spherical electrodes starts exactly at the pore ends, $x = \pm L/2$. Hence the potential along the pore axis turns to be

$$\frac{V(x)}{\Delta V} = \begin{cases} 1 - \frac{ad}{4(-x-L/2+d/2)} & x < -\frac{L}{2} \\ \frac{x}{L}(a-1) + \frac{1}{2} & -\frac{L}{2} < x < \frac{L}{2} \\ \frac{ad}{4(x-L/2+d/2)} & x > \frac{L}{2} \end{cases}, \tag{A12}$$

where $a = d/(2L+d)$. It is worth noting that the expression (A12) is written for the x axes but holds also for any electrical field line. Indeed, thanks to the spherical symmetry of the electrodes and the cylindrical symmetry of the pore, the electrical field lines are radial outside the pore and parallel to the x axes inside the pore. Therefore formula (A12) remains unchanged when the coordinate x runs along the pore axis or it is a curvilinear coordinate along a generic field line.

As a final remark, we report that the model can be refined describing the pore entrance not as spherical electrode but as planar disk as in Ref. [54]. We do not expect that the main conclusion of our work are affected by this improvement in the pore entrance model.

APPENDIX B: ENTROPIC CONTRIBUTION

When the rod arrives at the pore entrance, its positive tail is directed towards the pore and the allowed orientations can span a half sphere. When the rod is partially or fully inside the pore, a strong reduction on the allowed orientations occurs. As a first approximation we can estimate the entropic contribution

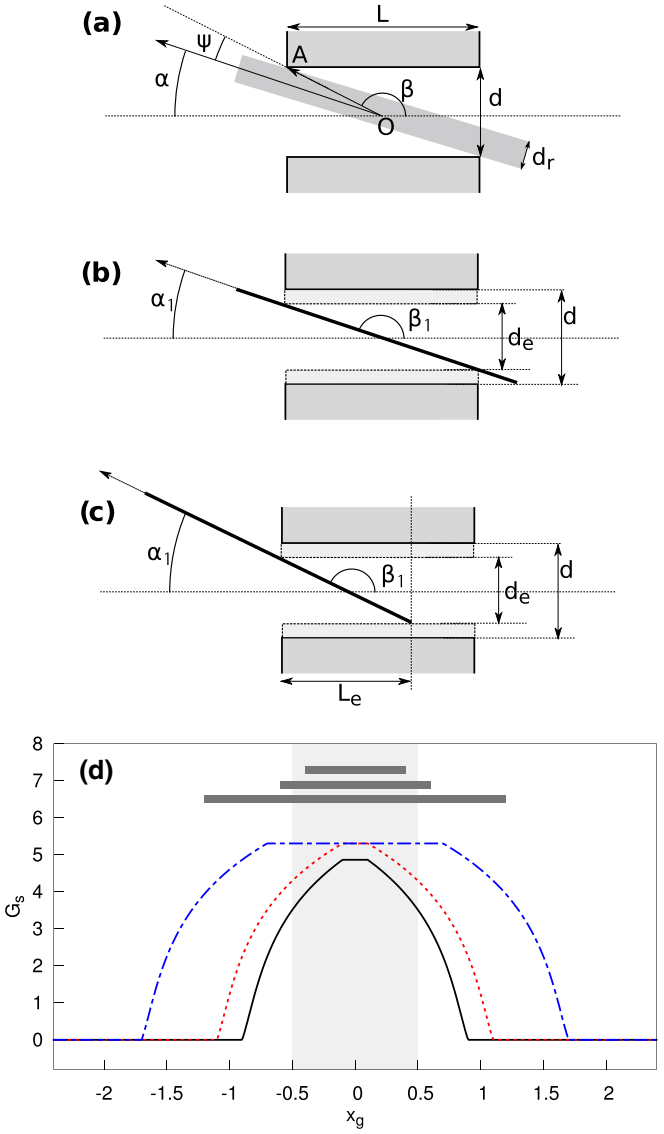

FIG. 7. (Color online) Allowed rod orientations. When the pore is completely filled by the rod the maximum angle α between the pore and the rod axes can be calculated as $\alpha = \pi - \beta - \psi$, where β and ψ are functions of the geometrical features of the pore (L and D) and of the rod (d_r), see panel (a). An approximated expression for α can be obtained considering a rod of zero thickness in a pore of effective diameter $d_e = d - d_r$ [panel (b)]. When the pore is only partially filled by the rod we can employ the same approach but considering an effective pore length L_e [panel (c)]. Panel (d) shows the entropic contribution for the three following cases: (blue dot-dashed line) $d = 0.2$, $L_r = 2.4$, $d_r = 0.1$; (red dashed line) $d = 0.2$, $L_r = 1.2$, $d_r = 0.1$; and (black solid line) $d = 0.2$, $L_r = 0.8$, $d_r = 0.1$.

to the free energy as

$$G_s(x_g) = -k_B T \log \frac{\Omega(x_g)}{2\pi}, \tag{B1}$$

where $\Omega(x_g)$ is the solid angle that a rod can explore when it is partially inside the pore [see Fig. 7(a)] and 2π is the solid angle that can be spanned when the rod has a terminal placed at the pore mouth. The function $\Omega(x_g)$ depends on the pore and the rod features. We derive here an approximation for the simplest case of a cylindrical rod of diameter d_r and length L_r inside a cylindrical pore of diameter d and length L.

Let us start considering the case when the pore is completely filled by the rod. The solid angle corresponding to the accessible orientations is $\Omega(x_g) = 2\pi(1 - \cos\alpha)$, where α is the maximum angle between the rod and the pore axis, it can be estimated calculating both the angles ϕ and β reported in Fig. 7(a). As a first approximation, the problem is equivalent to considering a rod of zero thickness in an effective pore of effective diameter $d_e = d - d_r$, hence we have [see Fig. 7(b)]

$$\Omega(x_g) = 2\pi(1 - \cos\alpha_1), \tag{B2}$$

$$\alpha_1 = \arccos\left[\frac{L}{\left(L^2 + d_e^2\right)^{1/2}}\right]. \tag{B3}$$

In the case of a pore partially occupied by the rod, we employed Eq. (B2) and Eq. (B3) with L replaced by the length of the occupied fraction of the pore [see Fig. 7(c)], in formulas,

$$L_e(x_g) = \int_{-\infty}^{+\infty} dx\ \Theta\left(\frac{L^2}{4} - x^2\right)\Theta\left[\frac{L_r^2}{4} - (x - x_g)^2\right], \tag{B4}$$

where Θ is the Heaviside step function. The resulting entropic contribution to the free-energy profile is reported in Fig. 7 for different rod geometries. It is worth mentioning, that these profiles are obtained under several assumptions and that their actual value is only to provide the order of magnitude of the entropic contribution.

[1] H. Bayley and P. S. Cremer, Nature **413**, 226 (2001).
[2] S. Majd, E. C. Yusko, Y. N. Billeh, M. X. Macrae, J. Yang, and M. Mayer, Curr. Opin. Biotechnol. **21**, 439 (2010).
[3] D. Rodriguez-Larrea and H. Bayley, Nat. Nanotechnol. **8**, 288 (2013).
[4] C. B. Rosen, D. Rodriguez-Larrea, and H. Bayley, Nature Biotechnology **32**, 179 (2014).
[5] E. L. Bonome, R. Lepore, D. Raimondo, F. Cecconi, A. Tramontano, and M. Chinappi, J. Phys. Chem. B **119**, 5815 (2015).
[6] L. Mereuta, M. Roy, A. Asandei, J. K. Lee, Y. Park, I. Andricioaei, and T. Luchian, Sci. Rep. **4**, 3885 (2014).
[7] L. Mereuta, A. Asandei, C. H. Seo, Y. Park, and T. Luchian, ACS Appl. Mater. Interfaces **6**, 13242 (2014).
[8] B. Cressiot, A. Oukhaled, L. Bacri, and J. Pelta, BioNanoScience **4**, 111 (2014).
[9] B.-j. Jeon and M. Muthukumar, ACS Macro Lett. **3**, 911 (2014).
[10] G. T. Feliciano, C. Sanz-Navarro, M. D. Coutinho-Neto, P. Ordejón, R. H. Scheicher, and A. R. Rocha, Phys. Rev. Appl. **3**, 034003 (2015).
[11] S. Howorka and Z. Siwy, Chem. Soc. Rev. **38**, 2360 (2009).
[12] M. Jain, I. T. Fiddes, K. H. Miga, H. E. Olsen, B. Paten, and M. Akeson, Nature Methods **12**, 351 (2015).
[13] E. A. Manrao, I. M. Derrington, A. H. Laszlo, K. W. Langford, M. K. Hopper, N. Gillgren, M. Pavlenok, M. Niederweis, and J. H. Gundlach, Nat. Biotech. **30**, 349 (2012).
[14] L. Mereuta, I. Schiopu, A. Asandei, Y. Park, K.-S. Hahm, and T. Luchian, Langmuir **28**, 17079 (2012).
[15] C. Madampage, O. Tavassoly, C. Christensen, M. Kumari, and J. Lee, Prion **6**, 116 (2012).
[16] M. Muthukumar, J. Chem. Phys. **132**, 195101 (2010).
[17] M. Bacci, M. Chinappi, C. Casciola, and F. Cecconi, J. Phys. Chem. B **116**, 4255 (2012).
[18] M. Bacci, M. Chinappi, C. M. Casciola, and F. Cecconi, Phys. Rev. E **88**, 022712 (2013).
[19] H. W. de Haan and G. W. Slater, Phys. Rev. Lett. **110**, 048101 (2013).
[20] A. Pelizzola and M. Zamparo, Europhys. Lett. **102**, 10001 (2013).
[21] J. Comer, V. Dimitrov, Q. Zhao, G. Timp, and A. Aksimentiev, Biophys. J. **96**, 593 (2009).
[22] A. B. Farimani, M. Heiranian, and N. R. Aluru, J. Phys. Chem. Lett. **6**, 650 (2015).
[23] D. Di Marino, E. L. Bonome, A. Tramontano, and M. Chinappi, J. Phys. Chem. Lett. **6**, 2963 (2015).
[24] N. Di Fiori, A. Squires, D. Bar, T. Gilboa, T. D. Moustakas, and A. Meller, Nat. Nanotechnol. **8**, 946 (2013).
[25] E. C. Yusko, J. M. Johnson, S. Majd, P. Prangkio, R. C. Rollings, J. Li, J. Yang, and M. Mayer, Nat. Nanotechnol. **6**, 253 (2011).
[26] P. Fanzio, C. Manneschi, E. Angeli, V. Mussi, G. Firpo, L. Ceseracciu, L. Repetto, and U. Valbusa, Sci. Rep. **2**, 791 (2012).
[27] M. Schiel and Z. S. Siwy, J. Phys. Chem. C **118**, 19214 (2014).
[28] D. P. Hoogerheide, B. Lu, and J. A. Golovchenko, ACS Nano **8**, 7384 (2014).
[29] S. W. Kowalczyk, D. B. Wells, A. Aksimentiev, and C. Dekker, Nano Lett. **12**, 1038 (2012).
[30] J. Nivala, D. B. Marks, and M. Akeson, Nat. Biotechnol. **31**, 247 (2013).
[31] A. Asandei, M. Chinappi, J.-k. Lee, C. H. Seo, L. Mereuta, Y. Park, and T. Luchian, Sci. Rep. **5**, 10419 (2015).
[32] M. Wanunu, W. Morrison, Y. Rabin, A. Y. Grosberg, and A. Meller, Nat. Nanotechnol. **5**, 160 (2009).
[33] M. Chinappi, C. M. Casciola, F. Cecconi, U. M. B. Marconi, and S. Melchionna, Europhys. Lett. **108**, 46002 (2014).
[34] U. Marini Bettolo Marconi and S. Melchionna, Langmuir **28**, 13727 (2012).
[35] F. Piguet, F. Discala, M.-F. Breton, J. Pelta, L. Bacri, and A. Oukhaled, J. Phys. Chem. Lett. **5**, 4362 (2014).

[36] Y. He, M. Tsutsui, C. Fan, M. Taniguchi, and T. Kawai, ACS Nano **5**, 5509 (2011).
[37] B. Luan and A. Aksimentiev, Phys. Rev. E **78**, 021912 (2008).
[38] P.-G. De Gennes, *Scaling Concepts in Polymer Physics* (Cornell University Press, Ithaca, NY, 1979).
[39] A. Y. Grosberg and A. Khokhlov, *Statistical Mechanics of Macromolecules* (AIP Press, Woodbury, NY 1994).
[40] M. Muthukumar, Polymers under confinement, in *Advances in Chem. Phys.* (John Wiley & Sons, New York, 2012), pp. 129–196.
[41] S. Kumar, J. M. Rosenberg, D. Bouzida, R. H. Swendsen, and P. A. Kollman, J. Comp. Chem. **13**, 1011 (1992).
[42] G. Hummer and A. Szabo, Acc. Chem. Res. **38**, 504 (2005).
[43] J. Kästner, WIREs: Computational Molecular Science **1**, 932 (2011).
[44] A. Ammenti, F. Cecconi, U. Marini Bettolo Marconi, and A. Vulpiani, J. Phys. Chem. B **113**, 10348 (2009).
[45] See Supplemental Material at http://link.aps.org/supplemental/10.1103/PhysRevE.92.032714 for additional data.
[46] A. Asandei, M. Chinappi, H.-K. Kang, C. H. Seo, L. Mereuta, Y. Park, and T. Luchian, ACS Appl. Mater. Interfaces, **7**, 16706 (2015).
[47] J. C. Phillips, R. Braun, W. Wang, J. Gumbart, E. Tajkhorshid, E. Villa, C. Chipot, R. D. Skeel, L. Kale, and K. Schulten, J. Comput. Chem. **26**, 1781 (2005).
[48] W. Humphrey, A. Dalke, K. Schulten *et al.*, J. Molec. Graphics **14**, 33 (1996).
[49] A. Aksimentiev, J. B. Heng, G. Timp, and K. Schulten, Biophys. J. **87**, 2086 (2004).
[50] G. Sigalov, J. Comer, G. Timp, and A. Aksimentiev, Nano Lett. **8**, 56 (2008).
[51] Y. Luo and B. Roux, J. Phys. Chem. Lett. **1**, 183 (2010).
[52] J. Gumbart, F. Khalili-Araghi, M. Sotomayor, and B. Roux, Biochim. Biophys. Acta Biomembr. **1818**, 294 (2012).
[53] M. R. Hossan, P. P. Gopmandal, R. Dillon, and P. Dutta, Electrophoresis **36**, 722 (2015).
[54] S. W. Kowalczyk, A. Y. Grosberg, Y. Rabin, and C. Dekker, Nanotechnology **22**, 315101 (2011).